

SOME ASPECTS OF THE ELASTIC ANISOTROPY OF SOLIDS

SHRIKANTH S.

Doctor of Philosophy



DEPARTMENT OF MATERIALS SCIENCE AND ENGINEERING

INDIAN INSTITUTE OF TECHNOLOGY DELHI

APRIL 2023

© Indian Institute of Technology Delhi (IITD), New Delhi, 2023

SOME ASPECTS OF THE ELASTIC ANISOTROPY OF SOLIDS

by

Shrikanth S.

Department of Materials Science and Engineering

Submitted in fulfilment of requirements of degree of
Doctor of Philosophy
to the



INDIAN INSTITUTE OF TECHNOLOGY DELHI

APRIL 2023

CERTIFICATE

This is to certify that the thesis entitled “**SOME ASPECTS OF THE ELASTIC ANISOTROPY OF SOLIDS**” is being submitted by **Mr. SHRIKANTH S.** to the Indian Institute of Technology Delhi for the award of the degree of **DOCTOR OF PHILOSOPHY**.

This is a record of bonafide research work carried out by him under our supervision and guidance. The matter presented in this thesis has not been submitted, in part or in full to any other University or Institute for the award of any degree or diploma.

Prof. Rajesh Prasad

Professor

Department of Materials Science and
Engineering

Indian Institute of Technology Delhi

Prof. Suresh Neelakantan

Associate Professor

Department of Materials Science and
Engineering

Indian Institute of Technology Delhi

Acknowledgements

This thesis is a result of studies that I carried out, along with my supervisors, over a period of five years. I express my sincere gratitude to my supervisors, Professor Rajesh Prasad and Professor Suresh Neelakantan for their guidance and support. On an equal note, I would like to thank Professor Kevin M. Knowles, of the Department of Materials Science and Metallurgy, University of Cambridge, for his guidance and encouragement. His sincerity and organised approach towards research made hard work look effortless and pushed me out of my comfort zone. I feel truly honoured to have worked with him.

The contents of this thesis are largely based on the concept of tensors which I picked up from the course ‘Micro and nanoscale mechanical behaviour of materials’ taught by one of my supervisors, Professor Rajesh Prasad, in my first year of Ph.D. Learning from him was the most delightful part of my Ph.D. experience. The innumerable open-ended discussions that we had over the years have greatly improved my understanding of various academic topics and shaped my views on becoming a better researcher. I am extremely thankful to him and his wife, Dr. Rachna Prasad, for their constant support, timely advice and the delicious meals at their home.

When I joined the institute, I was warmly welcomed to the ‘Materials Family’ by my labmates Aravi, Gaurav, Shanta, Aditya, Vicky, Prashant, Hemant and Anuz. They also got me trained in handling various testing equipment, gave valuable insights into Ph.D. life, and promoted a healthy work culture. We were further joined by a bunch of other enthusiastic researchers – Deepak, Ranjeet, Noor, Kasi, Amit, Chetan, Abhishek, Himanshu, Priyanka, Bushra, Ashwani, Ashitha, Karthik, Subhakar, Ayushi, Rashi, Amey, Surajbhan and Junaid. The lab was indeed a great workspace and I thank all my labmates and lab staff for their company and cooperation. I would also like to acknowledge the occasional enlightening discussions with Dr. Sarvesha from IIT Kanpur.

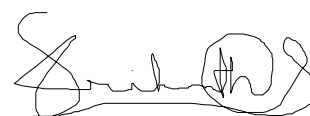
A good amount of my time at IIT Delhi was spent on the football field. Being a part of the institute football team was a parallel journey filled with joy, hard work and sacrifices. I would like to thank the coaches from Bhaichung Bhutia Football Schools and my wonderful teammates for the unforgettable memories that we made together.

Outside of the lab and football field, my stay at IIT Delhi was also enlivened by my friends – Sasi, Sriram, Rajeev, Della, Arshad, Chaithra, Nazil, Sasi Sir, Roshni, Abhimanyu, Amjad, Suraj, Saran, Kunjayi, Dhishana, Biyo, Abitha and Henna. Be it movies or the inevitable coffee breaks, these were the folks who were always around to ease things out.

Some friends are as good as family or even better. For me, Jessel, Divya and Ann have always had my back. These are people who celebrate my successes more than myself. They are also the ones who are more concerned about my difficulties than myself. I also have my brothers from NIT Rourkela close to my heart. Deekshith, Sarath, Vishnu, Sameeh, Vivek and Krishnan – they all kept visiting me in Delhi to roll back the years. I am sure none of them will accept a thanks from me. So, I leave it here.

Most importantly I wish to express my gratitude to my family. I was raised in a home with a father who stressed on the importance of logic and reasoning in daily life, a mother who held up affection and care over anything else, and an elder brother who competed against me for everything in the world. I am still driven forward by this mix of reasoning, love, and determination. As a child, I wanted to become a scientist, and my family has supported every decision that I have taken in that direction. Of late, I have not been able to spend as much time as I would have liked with them. Nevertheless, I have tried to make sure that the time spent away from them was being utilised justly.

I present my doctoral thesis ahead.



06/04/2023

SHRIKANTH S.

Abstract

In this thesis, new aspects of the anisotropy of the Poisson's ratio, shear modulus and biaxial modulus have been investigated. This study also includes the evaluation of an existing method of determining the Young's modulus of anisotropic materials using indentation measurements. Further, a new method to determine the elastic constants of cubic crystals from indentation measurements alone is proposed.

When a property or phenomenon varies with the direction of measurement, it is said to be anisotropic. Elastic properties of single crystals, layered/fiber-reinforced composites and textured polycrystals are few common examples of anisotropic materials. Random polycrystals, glasses and other amorphous materials are generally isotropic. The anisotropy of a material properties can be characterised using their tensor descriptions. The elastic response of linear elastic solids is governed by the Hooke's law. Stresses and strains are second-rank tensors while the stiffness/compliance constants are fourth-rank tensors.

Neumann's principle states that the symmetry elements of any physical property of a crystal must include the symmetry elements of the point group of the crystal. Therefore, the anisotropy of elastic properties of crystals are closely related to its symmetry. The anisotropy of properties like the Young's modulus (E), shear modulus (G) and Poisson's ratio (ν) have been extensively investigated. When the loading direction is confined within a plane with a three- or six-fold rotational symmetry, the Young's modulus has been reported to be invariant throughout the plane. The Poisson's ratio and shear moduli are also known to be invariant when the transverse plane and shear plane, respectively, possess a three-, four-, or six-fold symmetry. In the current study, it is found that transverse/shear planes without symmetry can also have invariant Poisson's ratio/shear modulus. Conditions on the elastic constants for the occurrence of such planes are identified and expressions for such plane normals are derived for all crystal systems.

The anisotropy in properties is observed in all forms of crystalline materials. Crystalline thin films deposited on substrates develop stresses and strains within the film. These stresses can be high and may result in the formation of defects or cracks. The actual states of stresses and strains within a film are not easily measurable. Hence, the biaxial modulus (B) is defined as the ratio of the in-plane tensile stress to the corresponding longitudinal strain under a state of equibiaxial strain or equibiaxial stress. It also appears in the Stoney equation which is used to determine the stresses in thin films from the measurement of its curvature. In the case of isotropic films, the biaxial modulus is given by $E/(1-\nu)$, and the states of equibiaxial strain and stress are equivalent. For anisotropic films, it is important to use the appropriate expressions for the biaxial modulus while determining the film stresses. The expressions for standard film orientations such as $\{001\}$, $\{110\}$ and $\{111\}$ of cubic films are known. In the current study, expressions for the biaxial moduli of thin films with a general (hkl) orientation are derived. Film planes within which the biaxial modulus remains independent of the direction of measurement are also identified for all crystal systems. An in-depth study on the case of cubic thin films is also carried out. The global extrema are identified and the expressions for the shear strains and out-of-plane normal strain are derived. The significance of the choice of boundary conditions is demonstrated by comparing the biaxial modulus derived under a zero shear strain state with that under a zero shear stress state.

The anisotropy of small-scale deformation processes can be studied using nanoindentation. Nanoindentation tests give a load-displacement ($P-h$) curve from which the contact stiffness can be estimated. The indentation modulus (M) is a property of the indented material and the geometry of the indenter. The indentation modulus of isotropic materials is the same as its plane strain Young's modulus which is given by $E/(1-\nu^2)$. In the case of anisotropic materials, M is a complicated function of the indented plane, elastic constants of the indented material, and the indenter geometry. A common practice is to use the isotropic

equation with the measured value of M and an assumed value of the bulk Poisson's ratio to determine the Young's modulus of anisotropic materials along the direction of indentation. The validity of such an approximation is examined in this study. It is found that $E_{(hkl)} = M_{(hkl)}(1 - \nu_{isotropic}^2)$ is highly likely to give reasonable results when the indented plane is either cubic {110} or any prismatic plane of hexagonal materials. In the case of other planes, the need to use appropriate equations accounting for the anisotropy is emphasised.

The elastic (stiffness/compliance) constants provide complete information regarding the elastic deformation response of solids. Relatively convenient and reliable methods like resonant ultrasound spectroscopy and Brillouin scattering are applicable to single crystalline specimens alone. Most of the materials with useful applications are polycrystals. However, simple, and effective methods to extract the elastic constants from polycrystalline specimens are not well established. Methods that combine nanoindentation measurements with electron backscatter diffraction (EBSD) have been developed to extract the elastic constants. Such methods either involve complex computations, use approximate relationships, or require the value of at least one bulk elastic property to be known/assumed. In the current study, approximate closed form expressions, with improved accuracy, are derived for the indentation moduli on the {100}, {110} and {111} planes of cubic materials. On identifying grains with these orientations within the polycrystal using EBSD, the indentation moduli can be measured, and the three independent elastic constants of the cubic crystallites are obtained.

सार

इस थीसिस में, पोयसन अनुपात, शियर मॉड्यूलस और बाईएक्सियल मॉड्यूलस की एनिसोट्रोपी के नए पहलुओं का अध्ययन किया गया है। इस अध्ययन में, एक विद्यमान विधि के माध्यम से एनिसोट्रोपिक माल के यंग मॉड्यूलस की निर्धारण की जांच भी शामिल है जो इंडेंटेशन मापनों का उपयोग करता है। इसके अलावा, एक नया तरीका प्रस्तावित किया गया है जिसके माध्यम से क्यूबिक क्रिस्टलों की लचीली संख्याएँ केवल इंडेंटेशन मापनों से निर्धारित की जा सकती हैं।

जब कोई गुणधर्म या घटना माप की दिशा से अलग-अलग होता है, तब इसे एनिसोट्रोपिक कहा जाता है। एकीकृत क्रिस्टल, तहती/फाइबर-बलगम संयोजन और बनावटयुक्त बहुक्रिस्टल की लचीली गुणधर्म कुछ एनिसोट्रोपिक माल के उदाहरण हैं। यादृच्छिक बहुक्रिस्टल, काँच और अन्य अमूर्त उपद्रव आमतौर पर इसोट्रोपिक होते हैं। एक वस्तु के गुणधर्मों की एनिसोट्रोपी का विवरण उनके टेंसर विवरणों का उपयोग करके किया जा सकता है। रॉयड के समान लचीले ठोस वस्तुओं का लचीला प्रतिसाद हूक का कानून द्वारा नियंत्रित किया जाता है। तनाव और तनाव परिवर्तन द्वितीय-श्रेणी के टेंसर होते हैं जबकि कठोरता / अनुपालन संयती निश्चित-श्रेणी के टेंसर होते हैं।

नेउमैन का सिद्धांत बताता है कि क्रिस्टल की किसी भी भौतिक गुणधर्म की सममिति उसके पॉइंट ग्रुप की सममितियों को शामिल करनी चाहिए। इसलिए, क्रिस्टल की कठोर गुणधर्मों की एनिसोट्रोपी उसकी सममिति से गंभीरता से जुड़ी होती है। यंग की मॉड्यूलस (E), शियर मॉड्यूलस (G) और पोइसन अनुपात (ν) जैसी गुणधर्मों की एनिसोट्रोपी का व्यापक अध्ययन किया गया है। जब लोडिंग दिशा को तीन- या छः-फोल्ड घुमावदार सममिति वाले एक समतल में सीमित किया जाता है, तब यंग की मॉड्यूलस का रिपोर्टेड वैरियंट समतल के अंतर्गत भी अचल होता है। पोइसन अनुपात और शियर मॉड्यूलस भी जाना जाता है कि जब त्रिविमानीय आयतन और काटने वाली तल, चार- चाहे या छह-फोल्ड सममिति के साथ होती है, तो पोइसन अनुपात और शियर मॉड्यूलस भी समान रहते हैं। वर्तमान अध्ययन में, यह पाया गया है कि बिना सममिति वाली ट्रांसवर्स/शियर तल भी अक्षम पोइसन अनुपात/शियर मॉड्यूलस को अक्षम कर सकते हैं। इस प्रकार के तलों के घटने के लिए केंद्रीय गुणों पर शर्तें पहचानी जाती हैं और सभी क्रिस्टल प्रणालियों के लिए ऐसे तलों के निर्धारण तत्वों को प्राप्त करने के लिए अभिव्यक्तियाँ निकाली जाती हैं।

गुणों में विषमता को क्रिस्टलीय सामग्रियों के सभी रूपों में देखा जाता है। परतों पर विकसित क्रिस्टलीय पतली फिल्मों में तनाव और तनाव पैदा होता है। ये तनाव अधिक हो सकते हैं और दोष या दरारों के गठन की वजह बन सकते हैं। फिल्म के भीतर तनाव और तनाव की वास्तविक स्थिति आसानी से मापने योग्य नहीं होती है। इसलिए, बिएक्सियल मॉड्यूलस (B) को इक्विबिएक्सियल तनाव या इक्विबिएक्सियल तनाव की स्थिति में चौड़ाई माप के अनुपात के रूप में परिभाषित किया जाता है। इसका उपयोग थिन फिल्मों के तनाव को उसकी घुमाव के माप से निर्धारित करने के लिए उपयोग में आता है। जैसे कि इसोट्रोपिक फिल्मों के मामले में, बिएक्सियल मॉड्यूलस $E/(1-\nu)$ द्वारा दिया जाता है, और समान दो-धारी तन और तनाव की स्थितियां समान होती हैं। एनिसोट्रोपिक फिल्मों के मामले में, फिल्म तनाव का निर्धारण करते समय बिएक्सियल मॉड्यूलस के उचित अभिव्यक्तियों का उपयोग करना महत्वपूर्ण होता है। घनवर्तुल फिल्मों के $\{001\}$, $\{110\}$ और $\{111\}$ जैसी मानक फिल्म अभिविन्यासों के लिए अभिव्यक्तियां जानी जाती हैं। वर्तमान अध्ययन में, एक सामान्य (hkl) अभिविन्यास वाली पतली फिल्मों के लिए बिएक्सियल मॉड्यूलस की अभिव्यक्तियां निकाली जाती हैं। सभी क्रिस्टल प्रणालियों के लिए, जिन फिल्म तनाव तथा तन की दिशा से निर्धारण की दिशा के अनुपात में बिएक्सियल मॉड्यूलस स्वतंत्र होता

है, उन फिल्मों की तल तालिका भी पहचानी जाती है। घनवर्तुल पतली फिल्मों के मामले पर भी एक विस्तृत अध्ययन किया जाता है। वैश्विक न्यूनतम तथा अधिकतम मान निर्धारित किए जाते हैं और कटाव तनों तथा तल तालिका के लिए अभिव्यक्तियां निकाली जाती हैं। सीमाओं के चयन की महत्वता, शून्य कटाव तन अवस्था तथा शून्य कटाव तनाव अवस्था के तहत प्राप्त बिएक्सियल मॉड्यूलस को तुलना करके दिखाई देती है।

नैनोइंडेंटेशन का उपयोग करके छोटे स्तर की विकर्षण प्रक्रियाओं की विभिन्नता का अध्ययन किया जा सकता है। नैनोइंडेंटेशन परीक्षणों से एक भार-विस्थापन ($P-h$) रुपरेखा दी जाती है, जिससे संपर्क स्टिफ़नेस का अनुमान लगाया जा सकता है। धातु की इंडेंटेशन मॉड्यूलस (M) एक गुण है, जो इंडेंटेशन के ज्यामिति तथा इंडेंटर के ज्यामिति के आधार पर निर्धारित होता है। इसोट्रोपिक सामग्री का इंडेंटेशन मॉड्यूलस उसके प्लेन स्ट्रैन यंग का मॉड्यूलस होता है ($E/(1-\nu^2)$)। द्विअभिमतीय सामग्रियों के मामले में, एम इंडेंटेशन की सतह, इंडेंटेड सामग्री के कसैतनीय संख्याओं, और इंडेंटर के ज्यामिति की एक जटिल फ़ंक्शन होता है। एक सामान्य अभ्यास है कि अभिमतीय सामग्रियों के यंग का मॉड्यूलस इसोट्रोपिक समीकरण का उपयोग करते हुए इंडेंटेशन की दिशा के अनुसार मापी जाती है। इस अध्ययन में ऐसी अनुमानित तकरीब की वैधता की जांच की गई है। यह पाया गया है कि जब इंडेंटेड प्लेन क्यूबिक {110} या हेक्सेगोनल सामग्री के किसी भी प्रिस्मात्मक तल पर हो तब वह उच्च रूप से उचित परिणाम देने के लिए बहुत संभावित होता है। अनुसूचितता के लिए उपयुक्त समीकरणों को उल्लेख करते हुए दूसरे तलों के मामले में एनिसोट्रोपी का खाता रखने की आवश्यकता पर जोर दिया गया है।

इलास्टिक कान्स्टन्टस (स्टिफ़नेस/कम्प्लाइअन्स) ठोस पदार्थों की लचीली उपचुंखता प्रतिक्रिया के संबंध में पूरी जानकारी प्रदान करते हैं। उल्लेखनीय आसान और विश्वसनीय तकनीकें जैसे रिसोनेंट अल्ट्रासाउंड स्पेक्ट्रोस्कोपी और ब्रिल्लुआँ स्कैटरिंग केवल एकल क्रिस्टल नमूनों के लिए उपयुक्त होती हैं। उपयोगी एप्लिकेशन वाले अधिकांश सामग्रियां बहुक्रिस्टल होती हैं। हालांकि, बहुक्रिस्टल नमूनों से लचीले निर्देशकों को निकालने के लिए सरल और प्रभावी तरीके अभी तक स्थापित नहीं हुए हैं। नैनोइंडेंटेशन मापनों को इलेक्ट्रॉन बैकस्कैटर डिफ़्रैक्शन (EBSD) के साथ मिलाकर लचीले निर्देशकों को निकालने के लिए तरीके विकसित किए गए हैं। ऐसे तरीकों में या तो जटिल गणनाओं का उपयोग करते हैं, अनुमानित संबंधों का उपयोग करते हैं या कम से कम एक बल्क लचीला गुणधर्म ज्ञात / माना जाना आवश्यक होता है। वर्तमान अध्ययन में, घन पदार्थों के {100}, {110} और {111} तलों पर इंडेंटेशन मॉड्यूलस के लिए समीकरणों को बेहतर निश्चितता के साथ बनाया गया है। EBSD का उपयोग करके पॉलीक्रिस्टल के भीतर इन अवस्थाओं के साथ अणुओं की पहचान करते हुए, इंडेंटेशन मॉड्यूलस को मापा जा सकता है, और घन त्रिज्या के तीन इलास्टिक कान्स्टन्टस को प्राप्त किया जा सकता है।

Table of Contents

Acknowledgements.....	ii
Abstract.....	iv
Table of Contents.....	ix
List of Figures.....	xv
List of Tables.....	xxi
List of Symbols.....	xxiv
Chapter 1 – Introduction.....	1
1.1 Generalised Hooke’s Law.....	2
1.2 Elasticity Tensors.....	4
1.2.1 Description of the Elastic Constants.....	5
1.3 Dependence of the Elastic Constants on Crystalline Symmetry.....	5
1.3.1 Point Groups.....	5
1.3.2 Neumann’s Principle.....	6
1.3.3 Forms of the Elasticity Matrices in Different Crystal Systems.....	6
1.4 Young’s modulus.....	12
1.4.1 Young’s Modulus Surface/Direction Surface and Direction Curves.....	13
1.4.2 Planes with Isotropic Young’s Modulus.....	16
1.5 Poisson’s Ratio.....	17
1.5.1 Areal Poisson’s Ratio.....	19
1.5.2 Representation of Poisson’s Ratio.....	20
1.6 Shear modulus.....	25
1.6.1 Representation of Shear Modulus.....	26
1.7 Polycrystalline Averages.....	29
1.7.1 The Voigt Average.....	31
1.7.2 The Reuss Average.....	31
1.7.3 The Voigt-Reuss-Hill Average.....	32

1.7.4 Other Averaging Methods.....	32
1.8 Anisotropy Parameters.....	33
1.8.1 Zener Anisotropy Parameter.....	33
1.8.2 Chung-Buessem Index.....	34
1.8.3 Ledbetter-Migliori Index.....	35
1.8.4 Universal Elastic Anisotropy Index.....	35
1.8.5 Log-Euclidean Anisotropy Parameter.....	37
1.8.6 Examples: Anisotropy Parameters of Various Crystals.....	37
1.9 Biaxial modulus.....	39
1.9.1 Polycrystalline Averages of Fiber-Textured Thin Films.....	41
1.10 Indentation Modulus.....	41
1.10.1 Indentation Modulus: Ambiguity in Literature.....	43
1.10.2 Indentation Modulus for a Flat Circular Punch on Anisotropic Materials.....	43
1.10.3 Indentation Modulus for Paraboloidal and Conical Indenters.....	45
1.10.4 Closed Form Expressions for the Indentation Moduli of Anisotropic Materials.....	48
1.11 Determination of Elastic Constants.....	51
1.11.1 Elastic Constants from Measurements on Single Crystals.....	51
1.11.2 Elastic Constants from Measurements on Polycrystals.....	52
1.11.3 Combined Usage of Nanoindentation and EBSD.....	53
Chapter 2 – Scope and Objectives.....	57
2.1 Research Gaps.....	57
2.1.1 Planes with Isotropic Properties in Anisotropic Materials.....	57
2.1.2 Stresses and Strains in Crystalline Films Deposited on a Substrate.....	57
2.1.3 Voigt and Reuss Bounds of the Biaxial Modulus of Fiber-textured Thin Films.....	58
2.1.4 Determination of the Elastic Properties of Anisotropic Solids from Indentation Measurements.....	58
2.2 Objectives.....	59
2.3 Organisation of the Thesis.....	60
Chapter 3 – Planes with Isotropic Poisson’s Ratio.....	61

3.1 Introduction.....	61
3.1.1 Isotropy of $\nu(\mathbf{n},\mathbf{m})$	61
3.1.2 Anisotropy Surfaces.....	61
3.2 Anisotropy of ν within a Plane.....	62
3.3 Poisson's Ratio Anisotropy Surfaces.....	66
3.4 Loading Directions where $\nu(\mathbf{n},\mathbf{m})$ is Independent of \mathbf{m}	69
3.4.1 Triclinic Crystals.....	70
3.4.2 Monoclinic Crystals.....	72
3.4.3 Orthorhombic Crystals.....	77
3.4.4 Trigonal Crystals.....	83
Point Groups 3 and $\bar{3}$	83
Point Groups 32, $\bar{3}m$ and $3m$	87
3.4.5 Hexagonal Crystals.....	92
3.4.6 Tetragonal Crystals.....	95
3.4.7 Cubic Crystals.....	104
3.5 Summary.....	106
Chapter 4 – Plane with Isotropic Shear Modulus.....	109
4.1 Introduction.....	109
4.1.1 Isotropy of $G(\mathbf{n},\mathbf{m})$	109
4.1.2 Anisotropy Surfaces.....	109
4.2 Anisotropy of G within a Plane.....	109
4.3 Shear Modulus Anisotropy Surfaces.....	112
4.4 Shear Planes where $G(\mathbf{n},\mathbf{m})$ is Independent of \mathbf{m}	114
4.4.1 Triclinic Crystals.....	115
4.4.2 Monoclinic Crystals.....	117
4.4.3 Orthorhombic Crystals.....	122
4.4.4 Trigonal Crystals.....	128
4.4.5 Hexagonal Crystals.....	137
4.4.6 Tetragonal Crystals.....	142

4.4.7 Cubic Crystals.....	151
4.5 Summary.....	152
Chapter 5 – Biaxial Modulus of Anisotropic Thin Films	155
5.1 Introduction.....	155
5.2 Stresses and Strains in Thin Films under Equibiaxial Strains.....	156
5.3 Expressions for the Biaxial Moduli under Equibiaxial Strain and Stress States.....	158
5.3.1 Biaxial Modulus under Equibiaxial Stress.....	158
5.3.2 Biaxial Modulus under Equibiaxial Strain.....	159
5.4 Biaxial Moduli of Cubic Thin Films under Equibiaxial Strain.....	161
5.4.1 $\{hkl\}$ Interface Orientations	161
5.4.2 $\{001\}$ Interface Orientations.....	166
5.4.3 $\{111\}$ Interface Orientations.....	167
5.4.4 $\{0kl\}$ Interface Orientations	167
5.4.5 $\{hhl\}$ Interface Orientations.....	169
5.5 Global Extrema of the Biaxial Modulus of Cubic Thin Films under Equibiaxial Strain.....	171
5.5.1 Stationary Points of the Principal Biaxial Moduli	171
5.5.2 Stationary Points of the Principal Biaxial Moduli on (Ok) Planes	175
5.5.3 Stationary Points and the Global Extrema of B_g	176
5.6 Expressions for the Strains ε_3^F , ε_4^F and ε_5^F in Cubic Thin Films under Equibiaxial Strain ...	180
5.6.1 Planes without Shear Strains.....	183
5.7 Comparison of the Biaxial Moduli under the Assumptions of Zero Shear Strains and Zero Normal Stresses	183
5.8 Summary.....	188
Chapter 6 – Anisotropy of the Polycrystalline Averages of the Biaxial Modulus of Fiber-Textured Thin Films.....	191
6.1 Introduction.....	191
6.2. Polycrystalline Averages of the Biaxial Modulus.....	194
6.2.1 The Voigt Average.....	194
6.2.2 The Reuss Average	195

6.3 Effective Biaxial Moduli Based on Average Polycrystalline Elastic Constants	196
6.4 Generalisation of the Kröner-Wawra Theorem for the Biaxial Modulus of Fiber-Textured Films	200
6.4.1 Cubic Crystals (All Point Groups)	202
6.4.2 Hexagonal Crystals (All Point Groups)	203
6.4.3 Tetragonal crystals	206
6.5 Planes with Isotropic Biaxial Moduli.....	208
6.5.1 Isotropy of Biaxial Modulus under an Equibiaxial Strain.....	208
6.5.2 Isotropy of Biaxial Modulus under an Equibiaxial Stress.....	208
6.5.3 Isotropic Planes in α -Dy, ZnO, BaTiO ₃ and YBCO	210
6.6 Representation Surfaces.....	214
6.7 Summary	218
Chapter 7 - Determination of Elastic Properties of Anisotropic Materials from Indentation	
Measurements	221
7.1 Introduction.....	221
7.2 Definitions of Important Terms and Basic Equations.....	222
7.2.1 Nanoindentation	222
7.2.2 Assessment of the Usage of $E = M(1 - \nu^2)$ for Anisotropic Materials	224
7.3 E_m / E Evaluated for Different Planes	226
7.3.1 Planes with Two-fold Symmetry	226
7.3.2 Planes with Three-fold Symmetry	228
7.3.3 Planes with Four-fold Symmetry	229
7.3.4 Planes with Six-fold Symmetry and Other Planes in Hexagonal Materials.....	230
7.3.5 E_m / E and Anisotropy Parameters.....	232
7.3.6 The Choice of ν in Eq. (7.5).....	236
7.4 Effect of Indenter Geometry on the Indentation Modulus on Planes with Two-fold Symmetry in Hexagonal and Cubic Materials.....	237
7.5 Approximate Closed-Form Expressions for the Indentation Moduli on {001}, {110} and {111}	242

7.5.1 Expression for $M_{\{001\}}$	242
7.5.2 Expression for $M_{\{110\}}$	243
7.5.3 Expression for $M_{\{111\}}$	246
7.5.4 Values of $M_{\{hkl\}}$ Predicted using the Approximate Closed-Form Expressions	247
7.6 Estimation of the Elastic Constants of Cubic Materials from Indentation Measurements	248
7.7 Limitations of Determining Elastic Constants from Nanoindentation Measurements.....	257
7.8 Summary	259
Chapter 8 – Conclusions and Future Work.....	261
8.1 Conclusions.....	261
8.2 Future Work.....	264
8.2.1 Planes with Isotropic Elastic Properties.....	264
8.2.2 Planes of Isotropy for Other Tensor-based Properties	264
8.2.3 Biaxial Moduli of Thin Films	265
8.2.4 Estimation of the Elastic Constants from Indentation Measurements	265
References.....	267
Appendix A.....	283
Appendix B	284
Appendix C.....	285
List of Publications	287

List of Figures

Figure 1.1 The new ($x'_1 - x'_2 - x'_3$) and old ($x_1 - x_2 - x_3$) coordinate systems, and the definitions of the angles θ , ϕ and ψ . M is the meridional tangent to the direction x'_3 while P is the projection of x'_3 on the $x_1 - x_2$ plane.....	3
Figure 1.2 The Young's modulus surfaces of (a) copper (cubic, $m\bar{3}m$), (b) molybdenum (cubic, $m\bar{3}m$), (c) zinc (hexagonal, $6/mmm$) and (d) titanium (hexagonal, $6/mmm$) (plotted by the author using Mathematica).....	15
Figure 1.3 The variations of the Young's moduli on the prismatic planes of (a) Zn (hexagonal, $6/mmm$) and (b) Ti (hexagonal, $6/mmm$) (plotted by the author using Mathematica)	16
Figure 1.4 The Young's moduli on the (a) (001), (b) (112), (c) (110) and (d) (111) planes of Cu and Mo, respectively (plotted by the author using Mathematica)	17
Figure 1.5 (a) Surfaces representing the extrema of the Poisson's ratio for each loading direction. The front views of the surfaces are shown in (b). (c) The extrema for each \mathbf{n} plotted against ϕ , the angle between \mathbf{n} and the c -axis (plotted by the author using Mathematica).....	21
Figure 1.6 (a) and (b) show the surfaces representing the extrema of Poisson's ratio for each loading direction in Cu and Mo, respectively. (b) The side views of the surfaces are respectively shown in (c) and (d) (plotted by the author using MATLAB).....	22
Figure 1.7 The variation of $\nu(\mathbf{n}, \mathbf{m})$ with \mathbf{m} when (a) \mathbf{n} is along the c -axis and (b) when \mathbf{n} lies in the basal plane of Zn. Positive values are shown in blue while the negative values are in red. A significant range of transverse directions can be seen to be auxetic when loaded along the basal plane (plotted by the author using MATLAB).....	23
Figure 1.8 $\nu(\mathbf{n}, \mathbf{m})$ (a) (001) section Cu (b) (001) section of Mo, (c) (111) section of Cu, (d) (111) section of Mo, (e) (110) section of Cu and (f) (110) section of Mo. Blue: positive values, red: negative values (plotted by the author using MATLAB)	24
Figure 1.9 (a) Surfaces representing the maximum (translucent blue) and minimum (solid green) shear moduli for each shear plane in indium (tetragonal). The top and side views are shown in (b) and (c) respectively. (d) Surface representing the average shear moduli for each shear plane in In. The top and side views are shown in (e) and (f) respectively (plotted by the author using MATLAB).....	27
Figure 1.10 The variations of $G(\mathbf{n}, \mathbf{m})$ along different shear planes in (a) Cu, (b) Zn, (c), In and (d) sillimanite (Al_2SiO_5). The arrows indicate one reference direction for the shear plane represented by the same colour (plotted by the author using MATLAB)	29
Figure 1.11 Schematic representation of a randomly textured polycrystalline specimen with cubic crystallites. The orientation of the cubes indicate the orientation of the grain. Any macroscopic direction (red lines) through the polycrystalline specimen encompasses grains with multiple	

orientations suggesting that it is likely to average out the values of the properties along all crystallographic directions	30
Figure 1.12 A schematic diagram of a thin film deposited on a substrate. Idealised cases where the in-plane tensile strains (or stresses) are equal are represented. The biaxial modulus along different directions within the film plane can be obtained by defining a new coordinate system rotated by an angle ψ about x_3^F	40
Figure 1.13 Schematic representation of the coordinate axes and symbols used in the calculation of the indentation modulus of anisotropic materials	45
Figure 1.14 Schematic representations of indentations by (a) a paraboloid of revolution and (b) a conical indenter. The projected contact ellipse and its orientation with respect to the $x_1 - x_2 - x_3$ Cartesian coordinate system is shown in (c).....	47
Figure 3.1 The variations of $\nu(\mathbf{n}, \mathbf{m})$ for different loading directions in ammonium tetroxalate dihydrate ($\text{NH}_4\text{H}_3(\text{C}_2\text{O}_4)_2 \cdot 2\text{H}_2\text{O}$, triclinic). The plot legend shows the Miller indices of the loading directions.....	66
Figure 3.2 Anisotropy surfaces with the radius proportional to $\Delta\nu(\mathbf{n})$: (a) Cu and (b) side view of Cu, (c) Mo and (d) side view of Mo. Inverted anisotropy surfaces with the radius proportional to $K_\nu - \Delta\nu(\mathbf{n})$: (e) Cu and (f) side view of Cu, (g) Mo and (h) side view of Mo.....	68
Figure 3.3 Surfaces representing the relative anisotropy of ν in ammonium tetroxalate dihydrate ($\text{NH}_4(\text{C}_2\text{O}_4)_2 \cdot 2\text{H}_2\text{O}$, triclinic, $\bar{1}$) with the radii proportional to (a) $\Delta\nu(\mathbf{n})$ (b) $K_\nu - \Delta\nu(\mathbf{n})$. The side views of the surfaces in (a) and (b) are shown in (c) and (d). The top views are shown in (e) and (f). Peaks in (b), (d) and (f) representing isotropic loading directions are marked by symbols given in Table 3.1 ..	70
Figure 3.4 Surfaces representing the relative anisotropy of ν in bismuth vanadate (monoclinic, $2/m$) with the radii proportional to (a) $\Delta\nu(\mathbf{n})$ (b) $K_\nu - \Delta\nu(\mathbf{n})$. The side views of the surfaces in (a) and (b) are shown in (c) and (d), respectively to highlight the symmetry two-fold symmetry about the x_2 axis. The top views are shown in (e) and (f) to highlight the mirror symmetry about the x_2 plane. Peaks in (b), (d) and (f) representing isotropic loading directions are marked by symbols given in Table 3.3. .	76
Figure 3.5 Surfaces representing the relative anisotropy of ν in caesium sulphate (orthorhombic, $\frac{2}{m} \frac{2}{m} \frac{2}{m}$) with the radii proportional to (a) $\Delta\nu(\mathbf{n})$ (b) $K_\nu - \Delta\nu(\mathbf{n})$. The side views of the surfaces in (a) and (b) are shown in (c) and (d), respectively. The top views are shown in (e) and (f). Peaks in (b), (d) and (f) representing isotropic loading directions are marked by symbols given in Table 3.6	82
Figure 3.6 Surfaces representing the relative anisotropy of ν in the ilmenite phase of magnesium silicate (MgSiO_3 , $\bar{3}$) with the radii proportional to (a) $\Delta\nu(\mathbf{n})$ (b) $K_\nu - \Delta\nu(\mathbf{n})$. The side views of the surfaces in (a) and (b) are shown in (c) and (d), respectively. The top views are shown in (e) and (f). Peaks in (b), (d) and (f) representing isotropic loading directions are marked by symbols given in Table 3.8	86

Figure 3.7 Surfaces representing the relative anisotropy of ν in calcite (CaCO_3 , trigonal, $\bar{3}m$) with the radii proportional to (a) $\Delta\nu(\mathbf{n})$ (b) $K_\nu - \Delta\nu(\mathbf{n})$. The side views of the surfaces in (a) and (b) are shown in (c) and (d), respectively. The top views are shown in (e) and (f). Peaks in (b), (d) and (f) representing isotropic loading directions are marked by symbols given in Table 3.10..... 91

Figure 3.8 Surfaces representing the relative anisotropy of ν in zinc (Zn, hexagonal, $6/mmm$) with the radii proportional to (a) $\Delta\nu(\mathbf{n})$ (b) $K_\nu - \Delta\nu(\mathbf{n})$. The side views of the surfaces in (a) and (b) are shown in (c) and (d), respectively. The top views are shown in (e) and (f). 94

Figure 3.9 Surfaces representing the relative anisotropy of ν in calcium molybdate (CaMoO_4 , $4/m$) with the radii proportional to (a) $\Delta\nu(\mathbf{n})$ (b) $K_\nu - \Delta\nu(\mathbf{n})$. The side views of the surfaces in (a) and (b) are shown in (c) and (d), respectively. The top views are shown in (e) and (f). Peaks in (b), (d) and (f) representing isotropic loading directions are marked by symbols given in Table 3.14 99

Figure 3.10 Surfaces representing the relative anisotropy of ν in indium (In, $4/mmm$) with the radii proportional to (a) $\Delta\nu(\mathbf{n})$ (b) $K_\nu - \Delta\nu(\mathbf{n})$. The side views of the surfaces in (a) and (b) are shown in (c) and (d), respectively. The top views are shown in (e) and (f). Peaks in (b), (d) and (f) representing isotropic loading directions are marked by symbols given in Table 3.16..... 102

Figure 4.1 Surfaces representing the relative anisotropy of G in Mo with the radii proportional to (a) $\Delta G(\mathbf{n})$ (b) $K_G - \Delta G(\mathbf{n})$. The front views of the surfaces in (a) and (b) are shown in (c) and (d) respectively. K_G is the difference in the shear moduli on the most anisotropic plane which is $\{110\}$ in this case..... 114

Figure 4.2 Surfaces representing the relative anisotropy of G in ammonium tetroxalate dihydrate ($\text{NH}_4\text{H}_3(\text{C}_2\text{O}_4)_2 \cdot 2\text{H}_2\text{O}$, triclinic point group $\bar{1}$) with the radii proportional to (a) $\Delta G(\mathbf{n})$ (b) $K_G - \Delta G(\mathbf{n})$. The side views of the surfaces in (a) and (b) are shown in (c) and (d) respectively to highlight the centre of inversion 116

Figure 4.3 Surfaces representing the relative anisotropy of G in bismuth vanadate (monoclinic, $2/m$) with the radii proportional to (a) $\Delta G(\mathbf{n})$ (b) $K_G - \Delta G(\mathbf{n})$. The side views of the surfaces in (a) and (b) are shown in (c) and (d), respectively to highlight the symmetry two-fold symmetry about the x_2 axis. The top views are shown in (e) and (f) to highlight the mirror symmetry about the x_2 plane 121

Figure 4.4 Surfaces representing the relative anisotropy of G in copper chloride dihydrate ($\text{CuCl}_2 \cdot 2\text{H}_2\text{O}$, $\frac{2}{m} \frac{2}{m} \frac{2}{m}$) with the radii proportional to (a) $\Delta G(\mathbf{n})$ (b) $K_G - \Delta G(\mathbf{n})$. The side views of the surfaces in (a) and (b) are shown in (c) and (d), respectively. The top views are shown in (e) and (f) 127

Figure 4.5 Surfaces representing the relative anisotropy of G in the ilmenite phase of magnesium silicate (MgSiO_3 , $\bar{3}$) with the radii proportional to (a) $\Delta G(\mathbf{n})$ (b) $K_G - \Delta G(\mathbf{n})$. The front views of the surfaces in (a) and (b) are shown in (c) and (d) respectively. The top views are shown in (e) and (f) to highlight the symmetry elements involving the x_3 axis 132

Figure 4.6 Surfaces representing the relative anisotropy of G in bismuth (Bi, trigonal, $\bar{3}m$) with the radii proportional to (a) $\Delta G(\mathbf{n})$ (b) $K_G - \Delta G(\mathbf{n})$. The front views of the surfaces in (a) and (b) are shown in (c) and (d) respectively. The top views are shown in (e) and (f) to highlight the symmetry elements involving the x_3 axis	136
Figure 4.7 Surfaces representing the relative anisotropy of G in zinc (Zn, hexagonal, $6/mmm$) with the radii proportional to (a) $\Delta G(\mathbf{n})$ (b) $K_G - \Delta G(\mathbf{n})$. The front views of the surfaces in (a) and (b) are shown in (c) and (d) respectively	140
Figure 4.8 Surfaces representing the relative anisotropy of G in magnesium (Mg, hexagonal, $6/mmm$) with the radii proportional to (a) $\Delta G(\mathbf{n})$ (b) $K_G - \Delta G(\mathbf{n})$. The front views of the surfaces in (a) and (b) are shown in (c) and (d) respectively	141
Figure 4.9 Surfaces representing the relative anisotropy of G in silver chlorate (AgClO_3 , point group $4/m$) with the radii proportional to (a) $\Delta G(\mathbf{n})$ (b) $K_G - \Delta G(\mathbf{n})$. The side views of the surfaces in (a) and (b) are shown in (c) and (d), respectively. The top views are shown in (e) and (f)	145
Figure 4.10 Surfaces representing the relative anisotropy of G in indium (In, $4/mmm$) with the radii proportional to (a) $\Delta G(\mathbf{n})$ (b) $K_G - \Delta G(\mathbf{n})$. The front views of the surfaces in (a) and (b) are shown in (c) and (d) respectively. The top views are shown in (e) and (f) to highlight the symmetry elements involving the x_3 axis.....	150
Figure 5.1 The biaxial modulus on the (234) and (129) planes in (a) Cu, (b) Si, (c) Nb and (d) β -brass. The variations of B (in GPa) with the angle ψ from the meridional tangent are shown. The principal stress axes on (234) and (129) are marked with blue dotted lines and red dot-dashed lines respectively	164
Figure 5.2 The variations of B with ψ on the (a) (001), (b) (111), (c) (012) and (d) (227) planes of Cu, Si, Nb and β -brass. The black lines at $\psi = 0^\circ$ and $\psi = 90^\circ$ correspond to the principal stress axes. The principal stress axes for (012) are $[02\bar{1}]$ and $[00\bar{1}]$. For the (227) plane, they are $[77\bar{4}]$ and $[\bar{1}10]$..	165
Figure 5.3 The variations of the principal biaxial moduli on planes of the type (0kl) in Cu, Si, Nb and β -brass as a function of the angle between the plane normal and [001]	168
Figure 5.4 The variation of the principal biaxial moduli on planes of the type (hhl) in Cu, Si, Nb and β -brass as a function of the angle between the plane normal and [001]	170
Figure 5.5 The out-of-plane normal strain ε_3^F (in terms of the in-plane equibiaxial strain $\varepsilon_{ }$) in (a) Cu and (b) Nb on planes of the type (hhl) and (0kl) plotted against the angle between the plane and (001).	181
Figure 5.6 The variations of the strains ε_3^F , ε_4^F and ε_5^F per unit $\varepsilon_{ }$ within the: (231), (012) and (227) planes of (a–c) Cu, and (d–f) Nb. The principal stress axes are indicated with vertical dashed lines.	182
Figure 5.7 The principal biaxial modulus B_1 plotted against α for the (012) planes of Cu and Nb. ...	187

Figure 6.1 B^V , B_ϵ^{eff} and B^R for different fiber textures in hexagonal materials: (a) graphite and (b) zinc.....	200
Figure 6.2 B^V , B_ϵ^{eff} and B^R for different fiber textures in α -dysprosium.....	204
Figure 6.3 The in-plane variations of B_ϵ and B_σ of $\text{CuSO}_4 \cdot 5\text{H}_2\text{O}$ on the (a) $(90^\circ, 43.694^\circ)$ plane and (b) the $(90^\circ, 94.173^\circ)$ plane showing that the biaxial moduli are isotropic on different planes.....	213
Figure 6.4 (a) The B_ϵ^{eff} and B^R surfaces for barium titanate (BaTiO_3 , tetragonal). The front views are shown in (b) and the top views in (c).....	214
Figure 6.5 (a) The B_ϵ^{eff} and (b) B^R surfaces for ZnO (hexagonal). The front views are shown in (b) and the top views in (c).....	215
Figure 6.6 B_ϵ^{eff} and B^R for different fiber textures of ZnO as a function of the angle (ϕ) between the fiber axis and the c -axis	216
Figure 6.7 (a) The B_ϵ^{eff} and (b) B^R surfaces for YBCO (orthorhombic). The front views are shown in (b) and the top views in (c)	217
Figure 6.8 (a) B_ϵ^{eff} and B^R for different fiber textures of YBCO as a function of the angle (ϕ) between the fiber axis and the c -axis: (a) when the fiber-axis lies in (100) and (b) when the fiber-axis lies in (010).....	217
Figure 7.1 The percentage distribution of E_m / E for planes with two-fold symmetry in different crystal systems	228
Figure 7.2 The percentage distribution of E_m / E for planes with three-fold symmetry in cubic and trigonal crystals.....	229
Figure 7.3 The percentage distribution of E_m / E for planes with four-fold (elastic) symmetry in cubic and tetragonal crystals.....	229
Figure 7.4 The percentage distribution of E_m / E for planes with six-fold symmetry in 152 hexagonal materials.....	230
Figure 7.5 The variations of E_m / E with the angle (ϕ) between the indented plane and the basal plane for 152 hexagonal materials.....	231
Figure 7.6 The distribution of planes in 152 hexagonal materials with different ranges of E_m / E ...	231
Figure 7.7 E_m / E values for the {100}, {111} and {110} planes plotted against the Zener anisotropy ratio (A) and the log-Euclidean anisotropy parameter (A^L) for 88 cubic materials	234
Figure 7.8 The ratio E_m / E plotted against the log-Euclidean anisotropy parameter (A^L) for 152 hexagonal materials on planes inclined to the basal plane at (a) 0° , (b) 10° , (c) 20° , (d) 30° , (e) 40° , (f) 50° , (g) 60° , (h) 70° , (i) 80° and (j) 90°	235

Figure 7.9 The E_m / E values for the {001}, {110} and {111} planes of the 88 cubic materials considered in this study obtained using $\hat{\nu}$ and ν_{VRH} 236

Figure 7.10 The ratio $M_{\{001\}}^{DU,C} / M_{\{001\}}^{VN,CP}$ plotted against the anisotropy parameter (A) for 87 cubic materials. The "correction factor" $\eta_{\{001\}}$ is obtained by fitting the curve with a power law expression 242

Figure 7.11 The ratio $M_{\{110\}}^{DU,C} / M_{\{110\}}^{VN,CP}$ plotted against the anisotropy parameter (A) for 87 cubic materials. The "correction factor" $\eta_{\{110\}}$ is obtained by fitting the curve with a power law expression 245

Figure 7.12 The values of E_m / E on the {111} planes of 88 cubic materials plotted against A . The equation of the fitted curve is also shown..... 246

Figure 7.13 The relative differences in the values of the indentation moduli on {001}, {110} and {111} planes predicted in the current study with respect to those calculated using the method of Vlassak & Nix (1994) plotted against A for 87 cubic materials 248

Figure 7.14 The Zener anisotropy ratio (A) of 88 cubic materials plotted against the ratio of indentation moduli on {111} and {001}: (a) materials with $A < 1$, (b) materials with $A > 1$ 253

List of Tables

Table 1.1 The elastic constants of Cu (cubic), Mo (cubic), Zn (hexagonal) and Ti (hexagonal) (Every & McCurdy, 1992). All values are in (TPa) ⁻¹	14
Table 1.2 Anisotropy parameters of a few crystals. Elastic constants reported in Every & McCurdy (1992) have been used for calculations.....	38
Table 3.1 All isotropic loading directions in ammonium tetroxalate dihydrate (NH ₄ (C ₂ O ₄) ₂ .2H ₂ O, point group $\bar{1}$) determined by minimizing $\Pi_2^2 + \Pi_3^2$	71
Table 3.2 Planes with isotropic Poisson's ratio in a few monoclinic materials.....	75
Table 3.3 Planes with isotropic Poisson's ratio in bismuth vanadate (BiVO ₄ , point group $2/m$)	75
Table 3.4 The constants q_i and p_i used to simplify the expression for θ in Eq. (3.33).....	79
Table 3.5 Planes with isotropic Poisson's ratio in a few orthorhombic materials.....	79
Table 3.6 Planes with isotropic Poisson's ratio in cesium sulphate (Cs ₂ SO ₄ , $\frac{2}{m} \frac{2}{m} \frac{2}{m}$)	81
Table 3.7 Planes with isotropic Poisson's ratio in a few trigonal materials (with point groups 3 and $\bar{3}$)	84
Table 3.8 Planes with isotropic Poisson's ratio in the ilmenite phase of magnesium silicate (MgSiO ₃ , $\bar{3}$)	87
Table 3.9 Planes with isotropic Poisson's ratio in a few trigonal materials (with point groups 32 , $3m$ and $\bar{3}m$).....	89
Table 3.10 Planes with isotropic Poisson's ratio in calcite (CaCO ₃ , $\bar{3}m$).....	90
Table 3.11 Planes with isotropic Poisson's ratio in a few hexagonal materials	93
Table 3.12 Planes with isotropic Poisson's ratio in zinc (Zn, $6/mmm$)	95
Table 3.13 Planes with isotropic Poisson's ratio in a few tetragonal crystals (point groups 4, $\bar{4}$ and $4/m$)	97
Table 3.14 Planes with isotropic Poisson's ratio in calcium molybdate (CaMoO ₄ , $4/m$).....	100
Table 3.15 Planes with isotropic Poisson's ratio in a few tetragonal crystals (point groups $4mm$, $\bar{4}2m$, 422 and $4/mmm$).....	101
Table 3.16 Planes with isotropic Poisson's ratio in indium (In, $4/mmm$).....	104
Table 3.17 Planes with isotropic Poisson's ratio in a few cubic crystals	105
Table 4.1 Planes with isotropic G in ammonium tetroxalate dihydrate (NH ₄ H ₃ (C ₂ O ₄) ₂ .2H ₂ O, triclinic point group $\bar{1}$) obtained by solving Eq. (3.16) using numerical methods. The corresponding isotropic values are also shown.....	117
Table 4.2 Planes with isotropic shear modulus in a few monoclinic materials	119
Table 4.3 Planes with isotropic shear modulus in bismuth vanadate (BiVO ₄ , point group $2/m$).....	122
Table 4.4 Planes with isotropic shear modulus in a few orthorhombic materials.....	126

Table 4.5 Planes with isotropic shear modulus in copper chloride dihydrate ($\text{CuCl}_2 \cdot 2\text{H}_2\text{O}$, $\frac{2}{m} \frac{2}{m} \frac{2}{m}$) ..	128
Table 4.6 Isotropic shear planes in a few trigonal materials (with point groups 3 and $\bar{3}$).....	130
Table 4.7 Planes with isotropic shear modulus in the ilmenite phase of magnesium silicate (MgSiO_3 , $\bar{3}$)	131
Table 4.8 Planes with isotropic shear modulus in a few trigonal materials (point groups 32, $3m$ and $\bar{3}m$)	135
Table 4.9 Planes with isotropic shear modulus in bismuth (Bi , $\bar{3}m$).....	135
Table 4.10 Planes with isotropic shear modulus in a few hexagonal materials	138
Table 4.11 Planes with isotropic shear modulus in zinc (Zn , $6/mmm$) and magnesium (Mg , $6/mmm$)	142
Table 4.12 Planes with isotropic shear modulus in a few tetragonal crystals (point groups 4, $\bar{4}$ and $4/m$)	144
Table 4.13 Isotropic shear modulus in silver chlorate (AgClO_3 , point group $4/m$)	144
Table 4.14 Planes with isotropic shear modulus in a few tetragonal crystals (point groups $4mm$, $\bar{4}2m$, 422 and $4/mmm$).....	148
Table 4.15 Isotropic shear planes in indium (In , $4/mmm$).....	149
Table 4.16 Planes with isotropic shear modulus in a few cubic crystals	151
Table 5.1 The principal stress axes and the corresponding principal biaxial moduli for the (234) and (129) planes in Cu, Si, Nb and β -brass	163
Table 5.2 Stationary points of the biaxial moduli in Cu, Si, Nb and Li. The global maxima are shown in bold, and the minima are underlined. The normals to the planes with the stationary points are of the form $(\theta = 45^\circ, \phi_{ij})$, where ϕ_{ij} are given by Eqs. (5.71) and (5.78). The stiffness values were obtained by inverting the compliance constants reported in Every & McCurdy (1992)	178
Table 6.1 Compliance s_{ij} constants of α -dysprosium, indium-lead alloy with 17 at.% Pb and strontium barium niobate ($\text{Sr}_{0.45}\text{Ba}_{0.55}\text{Nb}_2\text{O}_6$) from Every & McCurdy (1992). The stiffness constants c_{ij} calculated in the present work as the inverse of s_{ij} matrix are given	205
Table 6.2 The B^V and B^R (in GPa) of α -dysprosium (hexagonal), In-17 at.% Pb alloy and $\text{Sr}_{0.45}\text{Ba}_{0.55}\text{Nb}_2\text{O}_6$ (both tetragonal) with different fiber textures. The coinciding bounds are shown in bold	206
Table 6.3 Planes with isotropic biaxial modulus under equibiaxial strain and equibiaxial stress states	211
Table 6.4 B^V , B^R and B_ϵ^{eff} for different textures in YBCO.....	212

Table 7.5 The indentation moduli for different indenter geometries on the {110} planes of CuAuZn₂, Cu, Si, Mo and Nb calculated using the methods of Swadener & Pharr (2001) and Vlassak & Nix (1994). The values of ΔM_{VN} % are also shown..... 239

Table 7.6 The indentation moduli (in GPa) for different indenter geometries on the prismatic planes in different hexagonal materials: graphite, MoS₂, InN, GaN, BN, Zn, Ag₂Al, and Mg..... 241

Table 7.7 The indentation moduli on the {110} planes of cubic materials considered in Table 7.5 for a conical indenter – $M_{\{110\}}^{DU,C}$ predicted by Eq. (7.18) and $M_{\{110\}}^{SP,C}$ calculated using the method of Swadener & Pharr (2001). The relative differences between the two values are also shown..... 244

Table 7.8 Different c_{ij} values that give approximately the same indentation moduli along {001}, {110} and {111} as that of nickel. A and ν are dimensionless while all the other moduli are in GPa..... 250

Table 7.9 The Voigt-Reuss-Hill averages of the elastic properties of cubic crystals 251

Table 7.10 c_{ij} values obtained by the methods proposed in the current study using $M_{\{001\}} = 223$ GPa, $M_{\{110\}} = 243$ GPa and $M_{\{111\}} = 249$ GPa. The polycrystalline elastic moduli calculated using the determined c_{ij} are also shown. A and ν are dimensionless while all the other moduli are in GPa 252

Table 7.11 The stiffness constants of different materials determined by the method proposed in the current study along with the values reported in literature. The sources for the experimentally measured indentation moduli and the type of indenter used are also mentioned 255

Table 7.12 The experimentally measured values of the indentation moduli $M_{\{001\}}$, $M_{\{110\}}$ and $M_{\{111\}}$ and those calculated by the method of Vlassak & Nix (1994) using the c_{ij} determined in the current study (shown in Table 7.11)..... 256

List of Symbols

σ_{ij}	Stress field
σ_i	Stress field (matrix notation)
σ'_i	σ_i with respect to $x'_1 - x'_2 - x'_3$, a transformed coordinate system
ε_{ij}	Strain field
ε_i	Strain field (matrix notation)
ε'_i	ε_i with respect to $x'_1 - x'_2 - x'_3$, a transformed coordinate system
c_{ijkl}	Elastic stiffness tensor
s_{ijkl}	Elastic compliance tensor
c_{ij}	Elastic stiffness (matrix notation)
c'_{ij}	c_{ij} with respect to $x'_1 - x'_2 - x'_3$, a transformed coordinate system
s_{ij}	Elastic compliance (matrix notation)
s'_{ij}	s_{ij} with respect to $x'_1 - x'_2 - x'_3$, a transformed coordinate system
a_{ij}	Direction cosine matrix between the transformed ($x'_1 - x'_2 - x'_3$) and untransformed ($x_1 - x_2 - x_3$) coordinate systems
θ	Angle between x_1 and the projection of x'_3 on the $x_1 - x_2$ plane, for a coordinate transformation from the $x_1 - x_2 - x_3$ system to the new system ($x'_1 - x'_2 - x'_3$)
ϕ	Angle between x_3 and x'_3 , for a coordinate transformation from the old ($x_1 - x_2 - x_3$) system to the new system ($x'_1 - x'_2 - x'_3$)
ψ	Angle between the meridional tangent to x'_3 and x'_1 , for a coordinate transformation from the old ($x_1 - x_2 - x_3$) system to the new system ($x'_1 - x'_2 - x'_3$)
\mathbf{n}	Unit vector normal to the considered plane

\mathbf{m}	Unit vector perpendicular to \mathbf{n}
W	Elastic strain energy per unit volume
E	Young's modulus
$E_{(hkl)}$	Young's modulus along the normal to the plane (hkl)
E_m	Young's modulus obtained using the relationship between the Young's modulus, Poisson's ratio and the indentation modulus of isotropic materials
ν	Poisson's ratio
$\nu_{isotropic}$	Poisson's ratio of the polycrystalline sample
$\hat{\nu}$	Areal Poisson's ratio
G	Shear modulus
G^V	Voigt average of the shear modulus
G^R	Reuss average of the shear modulus
K	Bulk modulus
K^V	Voigt average of the shear modulus
K^R	Reuss average of the shear modulus
B	Biaxial modulus
B_σ	Biaxial modulus of thin films under equibiaxial stress
B_ε	Biaxial modulus of thin films under equibiaxial strain when there are no stresses acting normal to the film plane
\tilde{B}_ε	Biaxial modulus of films under equibiaxial strain when there are no shear strains
$B_\varepsilon^{(hkl)[uvw]}$	B_ε along $[uvw]$ when the film plane is (hkl)
B_ε^{eff}	New average biaxial modulus defined under the state of equibiaxial strain in fiber-textured thin films
B^R	Reuss average of the biaxial modulus of fiber-textured films
B^V	Voigt average of the biaxial modulus of fiber-textured films

M	Indentation modulus
$M_{(hkl)}$	Indentation modulus for an indentation normal to the plane (hkl)
$\langle c_{ijkl} \rangle$	Polycrystalline average of c_{ijkl}
$\langle s_{ijkl} \rangle$	Polycrystalline average of s_{ijkl}
c_{ijkl}^V	Voigt average of c_{ijkl}
s_{ijkl}^V	Voigt average of s_{ijkl}
c_{ijkl}^R	Reuss average of c_{ijkl}
s_{ijkl}^R	Reuss average of s_{ijkl}
c_{ijkl}^{VRH}	Voigt-Reuss-Hill average of c_{ijkl}
s_{ijkl}^{VRH}	Voigt-Reuss-Hill average of s_{ijkl}
A	Zener anisotropy parameter for cubic materials
A^*	Chung-Buessem anisotropy index
A^{LM}	Ledbetter-Migliori anisotropy index
A^U	Universal anisotropy index
A^L	Log-Euclidean anisotropy parameter
σ_{\parallel}	Equibiaxial normal stress acting parallel to the film plane
ε_{\parallel}	Equibiaxial normal strain acting parallel to the film plane
ε_{\perp}	Longitudinal strain acting normal to the film plane
P	Indentation load
h	Depth of indentation from the original undeformed surface

S	Contact stiffness
E_r	Reduced modulus of the indenter and indented material
A_p	Area of contact between the sample and indenter projected on to the specimen surface against the direction of indentation
E_i	Young's modulus of the indenter
ν_i	Poisson's ratio of the indenter
K_ν	Difference between the extreme values of the Poisson's ratio (ν) on the most anisotropic transverse plane of a given material
K_G	Difference between the extreme values of the shear modulus (G) on the most anisotropic shear plane of a given material
H	Elastic anisotropy parameter for cubic materials defined by Hirth and Lothe